# Vectorial point spread function and optical transfer function in oblique plane imaging

**Jeongmin Kim,[1,3] Tongcang Li,[2,3] Yuan Wang,[2,3] and Xiang Zhang[1,2,3,*]**

[1]*Department of Mechanical Engineering, University of California, Berkeley, California 94720, USA*
[2]*NSF Nanoscale Science and Engineering Center, 3112 Etcheverry Hall, University of California, Berkeley, California 94720, USA*
[3]*Materials Science Division, Lawrence Berkeley National Laboratory, 1 Cyclotron Road, Berkeley, California 94720, USA*
[*]*xiang@berkeley.edu*

**Abstract:** Oblique plane imaging, using remote focusing with a tilted mirror, enables direct two-dimensional (2D) imaging of any inclined plane of interest in three-dimensional (3D) specimens. It can image real-time dynamics of a living sample that changes rapidly or evolves its structure along arbitrary orientations. It also allows direct observations of any tilted target plane in an object of which orientational information is inaccessible during sample preparation. In this work, we study the optical resolution of this innovative wide-field imaging method. Using the vectorial diffraction theory, we formulate the vectorial point spread function (PSF) of direct oblique plane imaging. The anisotropic lateral resolving power caused by light clipping from the tilted mirror is theoretically analyzed for all oblique angles. We show that the 2D PSF in oblique plane imaging is conceptually different from the inclined 2D slice of the 3D PSF in conventional lateral imaging. Vectorial optical transfer function (OTF) of oblique plane imaging is also calculated by the fast Fourier transform (FFT) method to study effects of oblique angles on frequency responses.



**OCIS codes**: (260.1960) Diffraction theory; (180.0180) Microscopy; (110.0110) Imaging systems; (110.4850) Optical transfer functions.

## References and links

1. F. Anselmi, C. Ventalon, A. Bègue, D. Ogden, and V. Emiliani, "Three-dimensional imaging and photostimulation by remote-focusing and holographic light patterning," Proc. Natl. Acad. Sci. U.S.A. **108**(49), 19504–19509 (2011).
2. C. W. Smith, E. J. Botcherby, M. J. Booth, R. Juškaitis, and T. Wilson, "Agitation-free multiphoton microscopy of oblique planes," Opt. Lett. **36**(5), 663–665 (2011).
3. C. W. Smith, E. J. Botcherby, and T. Wilson, "Resolution of oblique-plane images in sectioning microscopy," Opt. Express **19**(3), 2662–2669 (2011).
4. W. Göbel and F. Helmchen, "New angles on neuronal dendrites in vivo," J. Neurophysiol. **98**(6), 3770–3779 (2007).
5. C. Dunsby, "Optically sectioned imaging by oblique plane microscopy," Opt. Express **16**(25), 20306–20316 (2008).
6. S. Kumar, D. Wilding, M. B. Sikkel, A. R. Lyon, K. T. MacLeod, and C. Dunsby, "High-speed 2D and 3D fluorescence microscopy of cardiac myocytes," Opt. Express **19**(15), 13839–13847 (2011).
7. F. Cutrale and E. Gratton, "Inclined selective plane illumination microscopy adaptor for conventional microscopes," Microsc. Res. Tech. **75**(11), 1461–1466 (2012).
8. E. J. Botcherby, R. Juskaitis, M. J. Booth, and T. Wilson, "Aberration-free optical refocusing in high numerical aperture microscopy," Opt. Lett. **32**(14), 2007–2009 (2007).
9. E. J. Botcherby, R. Juskaitis, M. J. Booth, and T. Wilson, "An optical technique for remote focusing in microscopy," Opt. Commun. **281**(4), 880–887 (2008).
10. C. J. R. Sheppard and H. J. Matthews, "Imaging in high-aperture optical systems," J. Opt. Soc. Am. A **4**(8), 1354–1360 (1987).
11. M. Gu, *Advanced Optical Imaging Theory* (Springer, 2000).
12. B. Richards and E. Wolf, "Electromagnetic Diffraction in Optical Systems. II. Structure of the Image Field in an Aplanatic System," Proc. R. Soc. Lond. A Math. Phys. Sci. **253**(1274), 358–379 (1959).

#207115 - $15.00 USD Received 25 Feb 2014; revised 8 Apr 2014; accepted 8 Apr 2014; published 1 May 2014

13. J. D. Jackson, *Classical Electrodynamics* (Wiley, 1999).
14. J. A. Stratton and L. J. Chu, "Diffraction Theory of Electromagnetic Waves," Phys. Rev. **56**(1), 99–107 (1939).
15. J. J. Stamnes, *Waves in Focal Regions: Propagation, Diffraction, and Focusing of Light, Sound, and Water Waves* (Adam Hilger, 1986).
16. T. D. Visser and S. H. Wiersma, "Spherical aberration and the electromagnetic field in high-aperture systems," J. Opt. Soc. Am. A **8**(9), 1404–1410 (1991).
17. C. J. R. Sheppard, A. Choudhury, and J. Gannaway, "Electromagnetic field near focus of wide-angular lens and mirror systems," IEEE J. Microwave Opt. Acoust. **1**(4), 129–132 (1977).
18. E. Wolf and Y. Li, "Conditions for the validity of the Debye integral representation of focused fields," Opt. Commun. **39**(4), 205–210 (1981).
19. Y. J. Li, "Focal shifts in diffracted converging electromagnetic waves. I. Kirchhoff theory," J. Opt. Soc. Am. A **22**(1), 68–76 (2005).
20. Y. J. Li, "Focal shifts in diffracted converging electromagnetic waves. II. Rayleigh theory," J. Opt. Soc. Am. A **22**(1), 77–83 (2005).
21. E. Wolf, "Electromagnetic diffraction in optical systems. I. An integral representation of the image field," Proc. R. Soc. Lond. A Math. Phys. Sci. **253**(1274), 349–357 (1959).
22. C. J. R. Sheppard, M. Gu, Y. Kawata, and S. Kawata, "Three-dimensional transfer functions for high-aperture systems," J. Opt. Soc. Am. A **11**(2), 593–598 (1994).
23. B. Frieden, "Optical Transfer of the Three-Dimensional Object," J. Opt. Soc. Am. **57**(1), 56–65 (1967).
24. C. J. R. Sheppard and K. G. Larkin, "Vectorial pupil functions and vectorial transfer functions," Optik (Stuttg.) **107**, 79–87 (1997).
25. M. R. Arnison and C. J. R. Sheppard, "A 3D vectorial optical transfer function suitable for arbitrary pupil functions," Opt. Commun. **211**(1-6), 53–63 (2002).

## 1. Introduction

Oblique plane microscopy (OPM) [1–7] images 2D cross-sections of a specimen that are tilted from the focal plane of a microscope objective lens. This microscopy has certain advantages in circumstances where an interested plane of a sample is inclined to conventional microscope's image plane [2–4], or biological processes of a living sample involve rapid changes in its structural orientation [2]. Compared to 3D scanning microscopy that typically extracts oblique planar information from slow 3D measurements, OPM provides a high-speed, cost-effective imaging method.

Commercial objective lenses satisfying the Abbe's sine condition suffer from optical aberrations if they are used to image any part of objects lying out of their focal planes. Remote focusing [8,9], which uses a second objective lens to cancel out these optical aberrations, provides a solution to form an aberration-free, 3D intermediate image of an out-of-focus object. Oblique plane imaging of this intermediate image is then conceptually feasible by employing another microscope with an inclined angle at the expense of partial use of its numerical aperture (NA) for detection, leading to resolution loss in an anisotropic manner.

Dunsby [5] has estimated the imaging resolution of oblique plane microscopy by approximating the full-width at half-maximum (FWHM) of the PSF from an effective NA concept, which is inaccurate and does not provide an analytical clue on non-isotropic lateral resolution. Anselmi *et al*. [1] proposed a wide-field oblique plane imaging method by a remote tilting technique, which has simpler configuration than Dunsby's. They explained qualitatively two mechanisms of resolution loss due to the possible light clipping and the inclined detection PSF. Because their experimental oblique angle was explored only up to 14° where such effect is small, no theoretical study on resolution was reported. On the other hand, Smith *et al*. [2,3] showed point-scanning oblique plane microscopy using a remote scanning technique. They studied non-isotropic lateral resolution for all oblique angles in terms of spatial cutoff frequencies deduced from the region of support for the 3D OTF in Fourier space. However, their analysis for point-scanning microscopy is not applicable to wide-field oblique plane imaging because their system has no light clipping with a different overall PSF. Accurate theoretical resolution of direct oblique plane imaging is thus still unclear.

In this paper, we theoretically calculate the accurate optical resolution of the wide-field oblique plane imaging for the first time. We derive a mathematical expression of the 3D pupil

#207115 - $15.00 USD Received 25 Feb 2014; revised 8 Apr 2014; accepted 8 Apr 2014; published 1 May 2014

function influenced by light clipping in any oblique angle between 0° and 90°. Then we calculate 2D intensity PSFs based on the vectorial diffraction theory that gives accurate results even for high NA systems (NA>0.6). FWHMs of the PSFs with different oblique angles are calculated to characterize the lateral resolution. We also calculate vectorial OTF from the FFT of the PSF to examine the effects of oblique angles on the spatial cutoff frequency.

## 2. Schematic of the oblique plane imaging

An oblique plane imaging system [1] is schematically shown in Fig. 1. The back focal planes of the two aplanatic objective lenses are relayed back-to-back by the L1-L2 optics. This layout compensates for aberrated optical wavefronts from the out-of-focus object near focal regions by the odd parity condition [8,9], thereby extending the depth of field [9]. Thus for an object lying within this range, the diffraction-limited 3D replica is formed in the remote space with a 3D isotropic magnification of the ratio of object/remote medium indices. The OBJ2-L3 constitutes another microscope to capture the oblique plane image of the remote object. Figure 1(a-c) shows that the $\alpha$-tilted plane ($x_\alpha y_\alpha$) in the object space is optically conjugate with the detector plane in the image space due to the $\alpha/2$-tilted mirror in the remote space. The pink beam in Fig. 1 shows how light is clipped at the OBJ2 induced by the tilted mirror. This light loss leads to a partial use of the OBJ2's exit pupil (the blue arc) and this rotationally asymmetric pupil yields an anisotropic resolving power. The NA or half-cone angle of the OBJ2 should be chosen greater than the mirror tilt angle, $\alpha/2$, to prevent a complete loss of light from detection. For example, an axial plane imaging ($\alpha = 90°$) requires NA greater than 0.71 in air medium. In general, the use of as high NA as possible is desirable to minimize the clipping of the signal light.

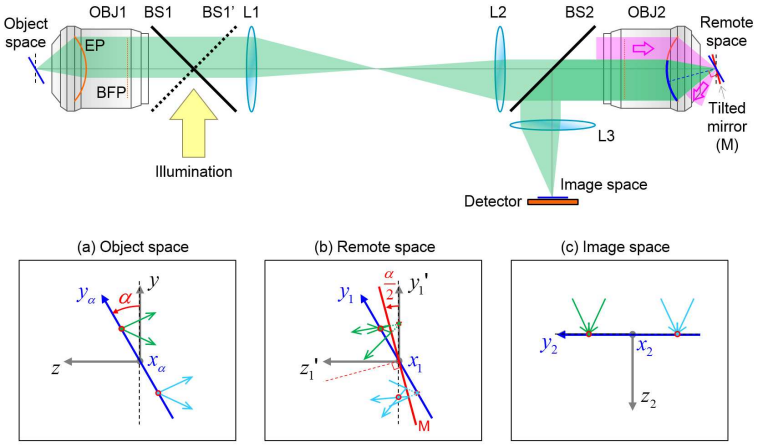


Fig. 1. Conceptual diagram of oblique plane imaging. OBJ: objective lens (EP: exit pupil; BFP: back focal plane); BS: beam splitter; L: lens; M: mirror. The beam path for an on-axis point object to the detector is shown in green, while the light clipping at the OBJ2 induced by the tilted mirror is illustrated in pink. Coordinates at (a) object space: an oblique plane ($x_\alpha y_\alpha$) inclined by $\alpha$ with respect to the focal plane ($xy$) of the OBJ1, (b) remote space: the $x_1y_1$ image plane conjugate with the $x_\alpha y_\alpha$ plane is rotated back to the $x_1'y_1'$ plane (the focal plane of the OBJ2) by the $\alpha/2$-tilted mirror, and (c) image space: the lateral detection plane ($x_2y_2$) is conjugate with the $x_\alpha y_\alpha$ object plane. Rays (green, light blue) from two points on the oblique $x_\alpha y_\alpha$ plane are focused on the $x_2y_2$ plane.

We note that the optical arrangement in Fig. 1 enables a 2D imaging of any oblique plane by controlling the tip-tilt of the small mirror M, of which size is about the working distance of the objective. In addition to this tip-tilt, a 3D translation of the mirror could also be realized to properly shift the image plane with neither specimen agitations nor additional optical

#207115 - $15.00 USD Received 25 Feb 2014; revised 8 Apr 2014; accepted 8 Apr 2014; published 1 May 2014

aberrations induced. Furthermore, the PSF in direct oblique plane imaging can be considered as a detection PSF in other types of oblique plane microscopy using either beam scanning or selective-plane illumination if the same light clipping is involved. For such a system, a variety of illumination methods among point-, line-scanning, light-sheet, and so on could be coupled through either BS1 or BS1' or other optical paths not shown in Fig. 1. The overall PSF of the imaging system then becomes the multiplication of the corresponding illumination and detection PSFs.

## 3. Theory and formulation

Classical scalar diffraction theory simplified with the Fresnel approximation is only applicable to low NA or paraxial imaging systems [10]. It loses its validity in high NA systems (NA>0.6) which we mainly deal with for oblique plane microscopy. Scalar Debye theory [11], which is a more advanced version of scalar diffraction theory, does not use the paraxial approximation and considers an apodization factor of high aperture systems. However, it still neglects the vectorial nature of the light. Depolarization [11] in high NA imaging system influences on the PSF, making its main lobe broader along the incident polarization direction than that predicted by the scalar Debye theory. To accurately predict the performance of oblique plane imaging for any oblique angle and NA regimes, we adopt the vectorial diffraction theory [12] that considers the polarization of electromagnetic waves.

### *3.1. Vectorial diffraction theory*

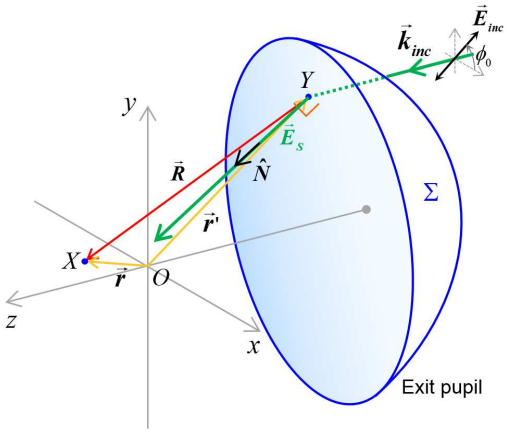


Fig. 2. Diffraction geometry. *O*: geometrical focus; *X*: an observation point; *Y*: a point on the exit pupil surface Σ where the incident field is refracted to $\vec{E}_s$. The distance $\overline{YX}$ is $R \equiv |\vec{r} - \vec{r}'|$.

Derived from a vector analogue of the Green's second identity, the vectorial Kirchhoff integral [13,14] for a time-independent electric field $\vec{E}$ at an observation point $\vec{r}$ is expressed in SI unit as

$$\vec{E}(\vec{r}) = \frac{1}{4\pi} \iint_{\Sigma} \left[ j\omega \left( \hat{N} \times \vec{B}_s \right) G + \left( \hat{N} \times \vec{E}_s \right) \times \nabla' G + \left( \hat{N} \cdot \vec{E}_s \right) \nabla' G \right] ds, \qquad (1)$$

where Σ is the wavefront surface over the exit pupil of an imaging system, $\hat{N}$ is a unit ray vector (normal to the wavefront), $\vec{E}_s$ and $\vec{B}_s$ are electric and magnetic fields respectively at the exit pupil, $\omega$ is the temporal frequency of the field, $G$ is the Green function of a diverging spherical wave $e^{ikR}/R$ with the distance $R$ shown in Fig. 2, $k$ is the wave number in medium, and $\nabla'$ is the gradient operator with respect to $\vec{r}'$. Applying Gauss's law, vector identities and assuming $k \gg 1/R$, Eq. (1) is reduced to

#207115 - $15.00 USD Received 25 Feb 2014; revised 8 Apr 2014; accepted 8 Apr 2014; published 1 May 2014

$$\vec{E}(\vec{r}) = \frac{-ik}{4\pi}\iint_{\Sigma} G\left[\vec{E}_S - \left(\vec{E}_S \cdot \hat{\vec{R}}\right)\hat{N} + \left(\hat{N}\cdot\hat{\vec{R}}\right)\vec{E}_S\right] ds. \tag{2}$$

In an aplanatic imaging system, parallel incident rays are assumed to refract at the spherical exit pupil towards the geometric focal point, making $\hat{N}$ and $-\vec{r}'$ parallel in Fig. 2. This aplanatic energy projection results in an angular apodization factor of $\cos^{\frac{1}{2}}\theta$ [15]. Assuming that there is no change in polarization angles upon the refraction itself, the complex amplitude of the field $\vec{E}_S$ is calculated on the geometric ground [16] as

$$\vec{E}_S = \cos^{\frac{1}{2}}\theta\left(\frac{(\hat{N}\times\vec{k}_{inc})\cdot\vec{E}_{inc}}{\left|(\hat{N}\times\vec{k}_{inc})\cdot\vec{E}_{inc}\right|}\cdot\frac{\hat{N}\times\vec{k}_{inc}}{\left|\hat{N}\times\vec{k}_{inc}\right|} + \frac{[(\hat{N}\times\vec{k}_{inc})\times\vec{k}_{inc}]\cdot\vec{E}_{inc}}{\left|[(\hat{N}\times\vec{k}_{inc})\times\vec{k}_{inc}]\cdot\vec{E}_{inc}\right|}\cdot\frac{(\hat{N}\times\vec{k}_{inc})\times\hat{N}}{\left|(\hat{N}\times\vec{k}_{inc})\times\hat{N}\right|}\right) \tag{3}$$

where $\vec{E}_{inc}$ is an incident electric field with a wavevector of $\vec{k}_{inc}$ (Fig. 2).

Assuming that the observation point is very close to the focal point *O* compared with the distance *R* in aplanatic systems, we can use the Debye approximation [17], i.e., $\vec{R} = \vec{r} - \vec{r}' \approx (\vec{r}\cdot\hat{N})\hat{N} - \vec{r}'$ . Then the vectorial Kirchhoff integral, Eq. (2), is further simplified to the vectorial Debye integral as

$$\vec{E}(\vec{r}) = \frac{e^{ikr'}}{i\lambda r'}\iint_{\Sigma}\vec{E}_S e^{ik\hat{N}\cdot\vec{r}}\, ds \tag{4}$$

where $\lambda$ is the wavelength in an immersed medium of which refractive index is $n$. The Debye approximation makes intensity distribution axially symmetric along the optical axis ($z$) and is valid if the Fresnel number $N_F = fNA^2/(n\lambda_0)$ is much greater than unity [18–20], where $f$ is the focal length and $\lambda_0$ is the vacuum wavelength. Most of the commercial objective lenses of any NA suffices $N_F > 100$. We confirmed from our numerical calculation that this criterion assures negligible axial shifts and an almost perfect match between Eq. (4) and (2) for any NA. Equation (4) also provides a different perspective of light propagation: a superposition of secondary plane wavelets [21], which are not conventional spherical wavelets.

Once the electric field is evaluated, the time-averaged electric energy density or intensity can be obtained by the modulus squared of the electric fields.

### *3.2. Pupil function in oblique plane imaging*

An evaluation of the vectorial Kirchhoff or Debye integrals requires a mathematical specification of the effective pupil area as conceptually explained in Fig. 1. In this section, we derive the normalized 3D pupil function $P(\theta,\phi)$ at the exit pupil of the object space in the spherical coordinate ($\theta$: polar angle, $\phi$: azimuthal angle). As illustrated in Fig. 3(a), an overlap between the original circular pupil area of the objective lens and its reflected pupil area by the $\alpha/2$-tilted mirror forms the effective pupil. We divide this circularly asymmetric pupil in oblique plane imaging into $\Sigma_1$ (rotationally symmetric part) and $\Sigma_2$ (the rest area) for mathematical convenience of the integral calculation. Appendix A includes more details. $\Sigma_1$ disappears at high $\alpha$ regime where $y_C > 0$ in Eq. (10). The pupil function for both $\Sigma_1$ and $\Sigma_2$ can be described as

$$P_{\Sigma_1}(\theta,\phi) = \begin{cases} 1, & \theta\in[0,\theta_C],\phi\in[0,2\pi],\, y_C < 0 \\ 0, & otherwise \end{cases} \tag{5}$$

$$P_{\Sigma_2}(\theta,\phi) = \begin{cases} 1, & \theta\in[\theta_C,\theta_{\max}],\phi\in[\phi_1(\theta),\phi_2(\theta)] \\ 0, & otherwise \end{cases} \tag{6}$$

#207115 - $15.00 USD Received 25 Feb 2014; revised 8 Apr 2014; accepted 8 Apr 2014; published 1 May 2014

where $\theta_C$, $\theta_{\max}$, $\phi_1(\theta)$, and $\phi_2(\theta)$ are defined in Appendix A. The bounds of $\theta$, $\phi$ are expressed as a function of $\alpha$, NA and $n$. Figure 3(c) shows several pupil functions that change with oblique angles.

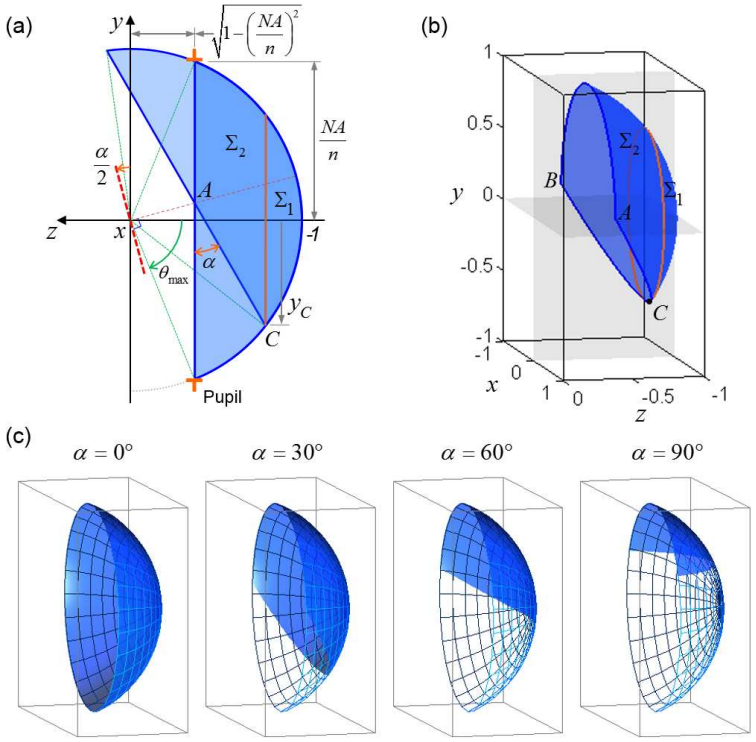


Fig. 3. (a) 2D and (b) 3D effective pupil geometry in the normalized object space. In (a), the circular pupil area of the objective lens and its mirror image by the $\alpha/2$-tilted virtual mirror (red dashed line) are illustrated. Their overlapped area forms the effective pupil. (c) Oblique angle dependence of the effective pupil shapes (NA = 1.4, $n$ = 1.52).

### *3.3. Point spread function*

To calculate the point spread function, we assume that an uniform electric field from a quasi-monochromatic, point source at infinity is incident to the exit pupil with a linear polarization angle of $\phi_0$ with respect to the $x$-axis, i.e., $\vec{\boldsymbol{E}}_{inc} = E_0(\cos\phi_0, \sin\phi_0, 0)$ in Fig. 2. The electric field near focal regions for the aplanatic oblique plane imaging system can be calculated from Eq. (4) (with the prefactor neglected) to be

$$\vec{\boldsymbol{E}}_{\phi_0}(x,y,z,) = \begin{pmatrix} E_{x,\phi_0} \\ E_{y,\phi_0} \\ E_{z,\phi_0} \end{pmatrix} = \iint_{\Sigma} \begin{pmatrix} \sin(\phi-\phi_0)\sin\phi + \cos(\phi-\phi_0)\cos\theta\cos\phi \\ -\sin(\phi-\phi_0)\cos\theta + \cos(\phi-\phi_0)\cos\theta\sin\phi \\ \cos(\phi-\phi_0)\sin\theta \end{pmatrix} \times \left(P_{\Sigma_1}(\theta,\phi) + P_{\Sigma_2}(\theta,\phi)\right)\cos^{\frac{1}{2}}\theta \times e^{-ik\left(x\sin\theta\cos\phi + y\sin\theta\sin\phi - z\cos\theta\right)} \sin\theta d\phi d\theta \tag{7}$$

Then the two-dimensional, in-focus intensity PSF (IPSF) over an oblique plane with a tilt angle $\alpha$ is

#207115 - $15.00 USD Received 25 Feb 2014; revised 8 Apr 2014; accepted 8 Apr 2014; published 1 May 2014

$$I_{\phi_0}(x_\alpha, y_\alpha) = \left| \begin{pmatrix} I_{x,\phi_0} \\ I_{y,\phi_0} \\ I_{z,\phi_0} \end{pmatrix} \right| = \left| \begin{array}{l} \iint_{\Sigma} \begin{pmatrix} \sin(\phi-\phi_0)\sin\phi + \cos(\phi-\phi_0)\cos\theta\cos\phi \\ -\sin(\phi-\phi_0)\cos\phi + \cos(\phi-\phi_0)\cos\theta\sin\phi \\ \cos(\phi-\phi_0)\sin\theta \end{pmatrix} \\ \quad \times \left( P_{\Sigma_1}(\theta,\phi) + P_{\Sigma_2}(\theta,\phi) \right) \cos^{\frac{1}{2}}\theta \\ \quad \times e^{-ik[x_\alpha \sin\theta\cos\phi + y_\alpha(\cos\alpha\sin\theta\sin\phi - \sin\alpha\cos\theta)]} \sin\theta d\phi d\theta \end{array} \right|^2 \tag{8}$$

For an unpolarized wave (see [12]), 2D IPSF can be derived as

$$I(x_\alpha, y_\alpha) = \frac{1}{2\pi}\int_0^{2\pi} \vec{E}_{\phi_0}^{*} \cdot \vec{E}_{\phi_0} d\phi_0 = \frac{1}{2}\left( \left|\vec{I}_A\right|^2 + \left|\vec{I}_B\right|^2 \right),$$

$$\vec{I}_j = \iint_{\Sigma_1+\Sigma_2} E_j e^{-ik[x_\alpha \sin\theta\cos\phi + y_\alpha(\cos\alpha\sin\theta\sin\phi - \sin\alpha\cos\theta)]} \sin\theta d\phi d\theta, \tag{9}$$

$$E_A = \cos^{\frac{1}{2}}\theta \begin{pmatrix} \sin^2\phi + \cos\theta\cos^2\phi \\ -\sin\phi\cos\phi + \cos\theta\sin\phi\cos\phi \\ \cos\phi\sin\theta \end{pmatrix}, E_B = \cos^{\frac{1}{2}}\theta \begin{pmatrix} -\sin\phi\cos\phi + \cos\theta\sin\phi\cos\phi \\ \cos^2\phi + \cos\theta\sin^2\phi \\ \sin\phi\sin\theta \end{pmatrix}$$

Both Eq. (8) and (9) are evenly symmetric with respect to $x_\alpha$ and $y_\alpha$. Thus a numerical calculation of any one quadrant is sufficient. For faster numerical calculation, Eq. (9) can be further modified to Eq. (15) in Appendix B.

### *3.4. Optical transfer function*

In low aperture scalar theory or Fourier optics where an imaging system is linear and space-invariant, OTF is the Fourier transform of PSF. In addition, analytical expressions for the 2D and 3D OTF for low aperture systems exist. The scalar Debye theory for circular, high aperture systems gives analytical 3D OTF. However, analytical 2D OTF does not exist and instead is numerically calculated from the projection of the 3D OTF [22]. No known explicit forms of 2D or 3D vectorial OTFs were found from our knowledge. On the other hand, they can be numerically calculated from either the Fourier transform of the vectorial PSF [23] or an autocorrelation of the vectorial pupil functions even for arbitrarily-shaped pupils [24,25]. Here we evaluate 2D vectorial OTFs for oblique plane imaging by performing the FFT of the 2D vectorial PSF to study the spatial cutoff frequency.

## 4. Numerical simulation results

The OBJ1 and the OBJ2 were considered as the same oil-immersion ($n$ = 1.52) objective lens. We considered three different cases of NA: 1.30, 1.40 and 1.49. The L1 and the L2 were considered identical. The light source was assumed to be a self-luminous, unpolarized, quasi-monochromatic ($\lambda_0$ = 519 nm), and isotropic point source. The Fresnel numbers of these high NA objective lenses are well above 1000, validating the Debye approximation.

### *4.1. Point spread function*

The 2D intensity PSFs obtained from the vectorial Debye integral, Eq. (15), are shown in Fig. 4. The PSF at $\alpha = 0°$ is equal to the conventional PSF of the circular aperture system of which resolution is isotropic in the lateral plane. The main lobe of the PSF stretches to the $y_\alpha$ direction more apparently at higher oblique angle due to the reduced pupil area, which results in an anisotropic lateral resolving power. This numerical simulation shows that there is also a slight PSF stretch along the $x_\alpha$ direction, which can be expected from the minor pupil loss along that direction as shown in Fig. 3(c). As a quantitative measure of these degradations,

#207115 - $15.00 USD Received 25 Feb 2014; revised 8 Apr 2014; accepted 8 Apr 2014; published 1 May 2014

the FWHM was calculated in Fig. 5. The optical resolution decreases when the oblique angle increases from $\alpha = 0°$ (conventional lateral imaging) to $\alpha = 90°$ (axial plane imaging) due to the reduced effective NA. The FWHM ratio of such two extreme angles at the NA of 1.30 (1.40, 1.49) is 1.33 (1.16, 1.06) and 4.39 (2.92, 2.09) along the $x_\alpha$- and $y_\alpha$-axis, respectively.

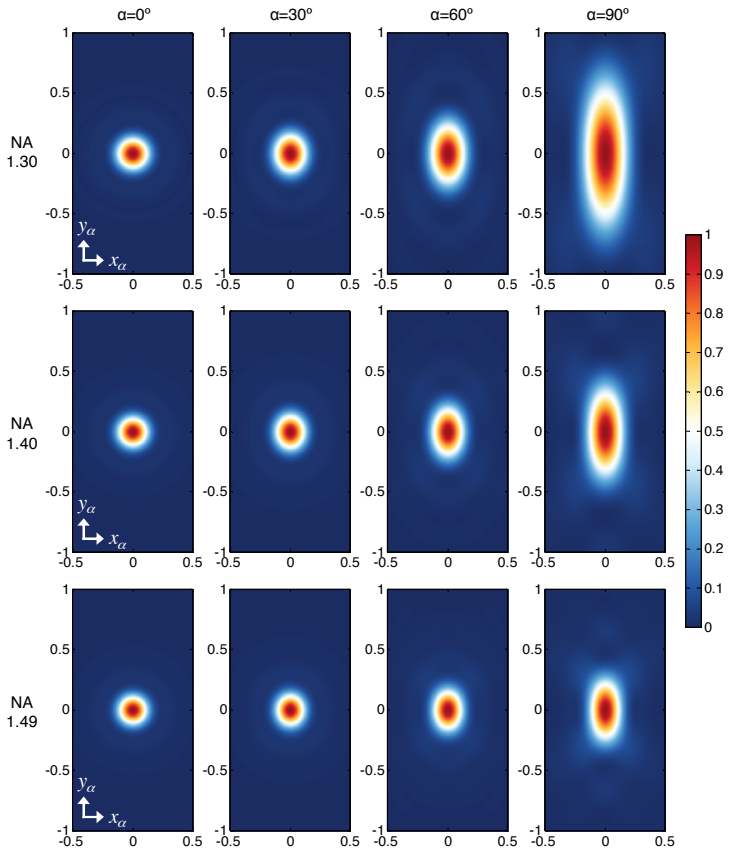


Fig. 4. 2D vectorial intensity PSF of the oblique plane imaging at different oblique angles ($\alpha$) and NAs, for $\lambda_0 = 519$ nm (unpolarized) and $n = 1.52$ (oil immersion). The axis unit is μm. The PSF elongates mainly along the vertical direction ($y_\alpha$) where the significant light clipping occurs in oblique plane imaging. Higher NA makes such an anisotropic resolving power less sensitive to the oblique angle.

We also compared our results of FWHMs in oblique plane imaging with those calculated from the inclined PSF. For the inclined PSF, as shown in the inset in Fig. 5, the 3D vectorial PSF from a conventional circular aperture system was rotated about the $x$-axis to calculate a FWHM for each inclination α. While this rotation keeps the FWHM along the $x$-axis unchanged (green dashed curve), it gives certain FWHM deterioration along the $y$-axis (green line curve) originated from the well-known "ellipsoidal" PSF. Thus the rate of the increase in $FWHM_y$ calculated from the inclined PSF slows down near 90° and the FWHM converges to the $FWHM_z$ of the 3D PSF. This nature is quite different from the sharp increase near 90° in our simulation results together with the FWHM along the $y_\alpha$-axis at $\alpha = 90°$ not limited to the $FWHM_z$ of the conventional PSF. It is clear that the tilt of the conventional PSF fails to predict both the minor $x$-resolution loss and the $y$-resolution trend over the oblique angles, both of which are attributed to the pupil area loss from the light clipping. This result tells that the inclined slice of the conventional 3D PSF is different from the light-clipped 2D PSF that we calculated.

#207115 - $15.00 USD Received 25 Feb 2014; revised 8 Apr 2014; accepted 8 Apr 2014; published 1 May 2014

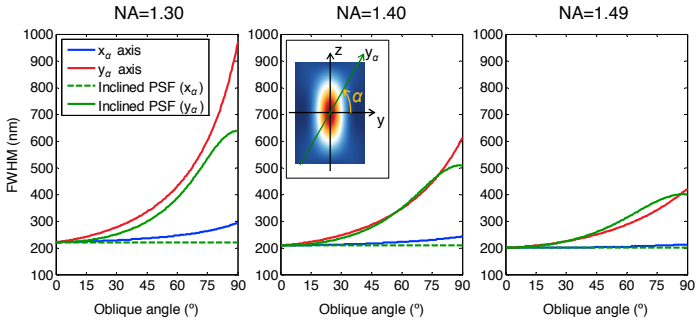


Fig. 5. FWHM of the vectorial PSFs at different NA values along the $x_\alpha$- and $y_\alpha$-axis over the oblique angle. For comparison, the FWHM from the inclined 3D vectorial PSF of the circular aperture system (the inset in the middle) is also plotted.

### *4.2. Optical transfer function*

We first verified an accuracy of OTF calculated by the FFT method. For the scalar Debye 2D OTF for a circular aperture system ($\alpha = 0°$), we can calculate it by either the FFT of the scalar Debye 2D PSF or the 2D projection of the analytical scalar Debye 3D OTF. We compared the OTFs obtained from both methods in Fig. 6. It was found that in the FFT method PSF data with a sufficient number of sidelobes is essential for accurate results: although higher sidelobes have several orders of magnitude lower intensity than the peak intensity of the main lobe, they still contribute much on OTF curves especially at low-to-middle spatial frequency regimes. Utilizing 2D PSF data containing up to 25 sidelobes along both the $x$ and $y$ directions led to a good agreement between numerical (FFT-based) and analytical (2D projected) OTFs: black vs. red curve in Fig. 6(b). The relative error in modulation transfer function (MTF) value was smaller than 0.013 over the entire spatial frequency. A numerical OTF from the PSF with 60-sidelobes almost perfectly overlapped with the analytical one, but this required about six times more computational time.

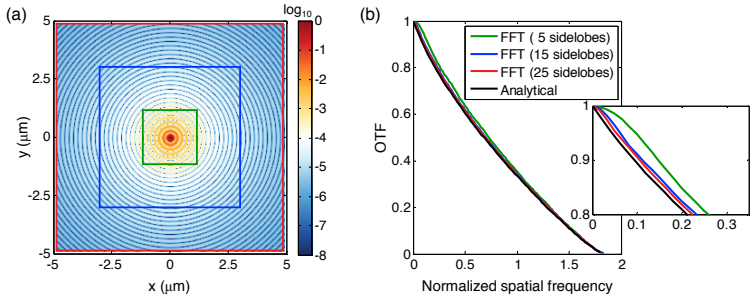


Fig. 6. (a) Scalar Debye intensity PSF used to calculate an OTF by FFT (NA = 1.4, $n$ = 1.52, $\lambda_0$ = 519nm, $\alpha$ = 0°). The green, blue and red rectangles contain 5, 15 and 25 sidelobes respectively. (b) A comparison between FFT-based and analytical scalar Debye OTFs in the normalized spatial frequency by $n/\lambda_0$. The PSF with enough sidelobes is necessary for an accurate OTF calculation. The inset shows details near the low frequency regimes.

After confirming the accuracy of our FFT-based method, we numerically calculated the vectorial OTF in oblique plane imaging which has no analytical solution. We evaluated Eq. (15) in MATLAB's parallel computing environment to obtain the vectorial 2D PSF data with 25-sidelobes along the $x_\alpha$ and $y_\alpha$ directions, followed by the 2D FFT operation. Figure 7 shows the 2D vectorial OTF of direct oblique plane imaging on the spatial frequency coordinates $m_x$-$m_y$ (normalized by $n/\lambda_0$), which correspond to the $x_\alpha$ and $y_\alpha$ directions in real space. As the oblique angle increases, the bandwidth (or cutoff frequency) along the $m_y$-direction shrinks much faster than that along the $m_x$-direction, which is qualitatively self-

#207115 - $15.00 USD Received 25 Feb 2014; revised 8 Apr 2014; accepted 8 Apr 2014; published 1 May 2014

explanatory from the anisotropic PSFs in Fig. 4. Cross-sections of those OTFs were examined in Fig. 8. For $\alpha = 0°$, compared with the scalar Debye OTFs, the vectorial OTFs have lower modulation over the spatial frequency range. This MTF degradation is caused mainly by the depolarized light component along the optical axis that induces PSF broadening, which is neglected in the scalar theory. On the other hand, the cutoff frequency in the scalar Debye theory is $2NA/n$, i.e., 1.71 (1.84, 1.96) for the NA of 1.30 (1.40, 1.49), corresponding to 5.0 (5.4, 5.7) cycles/μm in physical coordinate. We determined the numerical cutoff frequency of the vectorial OTF at a threshold MTF of 0.01% to ignore the minor MTF oscillations (numerical artifacts) occurring near and above the cutoff frequency. The calculated vectorial cutoff frequencies for $\alpha = 0°$ were consistent with the analytical scalar Debye cutoffs within 1% error.

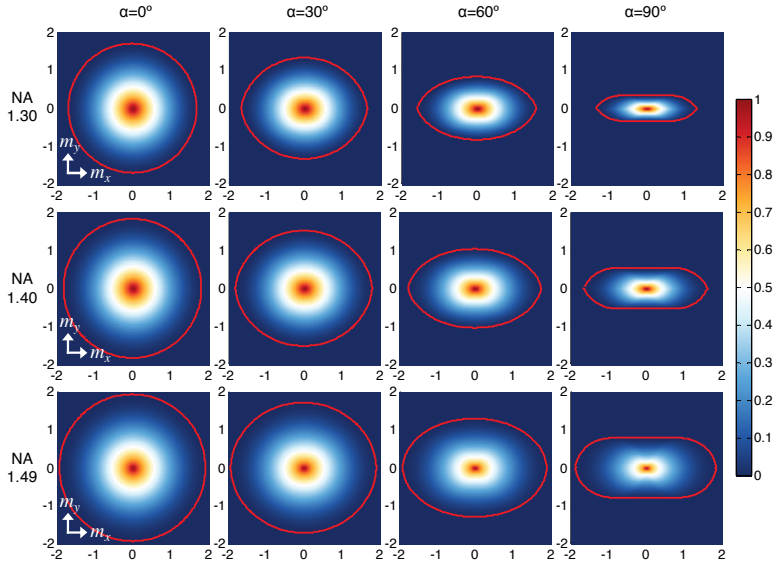


Fig. 7. 2D vectorial OTF of the oblique plane imaging at different oblique angles ($\alpha$) and NAs ($\lambda_0$ = 519 nm, $n$ = 1.52). The MTF cutoff contours are drawn in red. The lateral coordinate is normalized by $n/\lambda_0$.

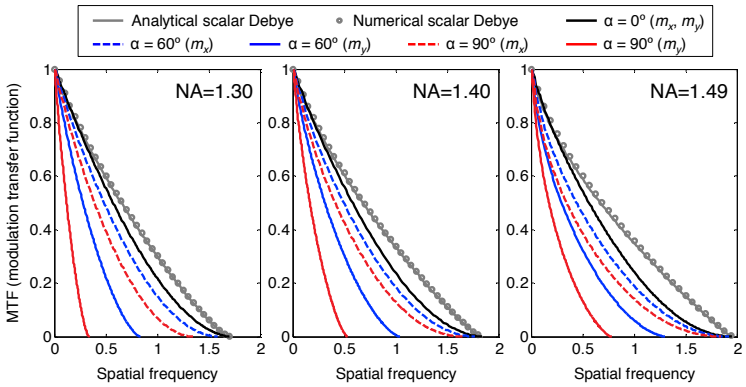


Fig. 8. Vectorial OTF cross-sections along the horizontal ($m_x$) and vertical ($m_y$) directions for $\alpha$ = 0, 60, and 90°. The scalar Debye OTF (both analytical and numerical) for $\alpha = 0°$ is also plotted for comparison. The spatial frequency is normalized by $n/\lambda_0$ ($\lambda_0$ = 519 nm, $n$ = 1.52).

From the OTF cross-sections for $\alpha$ = 60, 90° in Fig. 8, we clearly see a downward trend in both MTF value and cutoff frequency with the oblique angle. This change is plotted in Fig. 9.

#207115 - $15.00 USD Received 25 Feb 2014; revised 8 Apr 2014; accepted 8 Apr 2014; published 1 May 2014

The cutoff frequency along the $m_x$ axis drops by 21% (10%, 5%) for the NA of 1.30 (1.40, 1.49) as the oblique angles increases from 0° to 90°. Similarly, the $m_y$ cutoff frequency reduces up to 80% (71%, 60%). The cutoff frequency declines quantitatively less for lenses with higher NA.

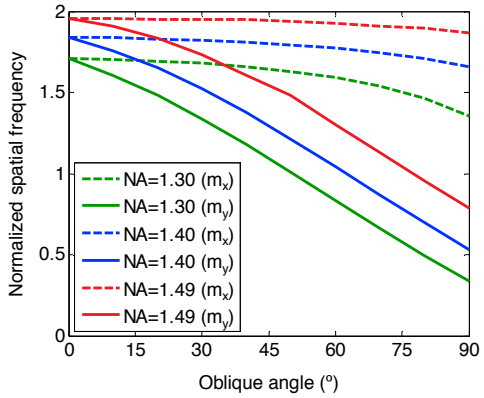


Fig. 9. The variation in the cutoff frequency of the vectorial OTF along the horizontal ($m_x$) and vertical ($m_y$) directions over the oblique angle.

## 5. Conclusion and discussion

Oblique plane imaging using the remote tilting method provides direct 2D images of any oblique plane of interest in 3D samples. Despite its innovative method of wide-field imaging, no comprehensive study on the anisotropic change in optical resolution upon the oblique angle due to the light clipping has been reported. Here we investigated this behavior quantitatively by calculating the vectorial PSF and OTF using the vectorial diffraction theory. Despite such variations in resolution more sensitive at higher oblique angles, sub-μm lateral resolution is still attainable at higher NA with visible light. The direct 2D imaging capability of any oblique angle that is controllable would prevail over the variable resolution in many biological studies. Also, we found that the oblique slice of the conventional 3D PSF based on a circular pupil does not explain the 2D PSF in wide-field oblique plane imaging.

The effect of the light clipping on the resolving power could be neglected for the low oblique angle regime. In our numerical simulations, the PSF's FWHM increases along the mirror-tilt direction less than 10% for the oblique angle up to 16° (20°, 27°) for the NA of 1.30 (1.40, 1.49) in oil medium at the vacuum wavelength of 519 nm. Here, we assumed a uniformly incident electric field to the exit pupil with a perfectly unpolarized state. In an experimental attempt to measure the detection PSF with a fluorescent point object, what has to be isolated are the finite size of the object convolved into the PSF and the properties of dipole radiation or scattering of the object [24].

We emphasize that our PSF formulation is not restricted to the wide-field oblique plane imaging. It can be used to obtain the detection PSF for other methods of oblique plane imaging as long as they undergo similar light clipping caused by a tilted optical component.

## Appendix A. Derivation of the point *C* coordinate and the bounds of the pupil function

In Fig. 3, the equation of the plane ABC is $y - z\cot\alpha - \sqrt{1-(NA/n)^2}/\sin\alpha = 0$. Plugging this equation into the unit sphere equation ($x^2 + y^2 + z^2 = 1$ with $x = 0$) gives the coordinate values of the point *C* as

$$\left(x_C, y_C, z_C\right) = \left(0, -\frac{NA}{n}\cos\alpha + \sqrt{1-\left(\frac{NA}{n}\right)^2}\sin\alpha, -\frac{NA}{n}\sin\alpha - \sqrt{1-\left(\frac{NA}{n}\right)^2}\cos\alpha\right). \quad (10)$$

#207115 - $15.00 USD Received 25 Feb 2014; revised 8 Apr 2014; accepted 8 Apr 2014; published 1 May 2014

With a Cartesian-to-spherical coordinate relation defined by $(x, y, z) \equiv (\sin\theta\cos\phi, \sin\theta\sin\phi, -\cos\theta)$, the bounds of the pupil area are given by

$$\theta_C = \cos^{-1}\left|z_C\right| = \cos^{-1}\left|\frac{NA}{n}\sin\alpha + \sqrt{1-\left(\frac{NA}{n}\right)^2}\cos\alpha\right|, \tag{11}$$

$$\theta_{\max} = \sin^{-1}\left(\frac{NA}{n}\right), \tag{12}$$

$$\phi_1(\theta) = \sin^{-1}\left(\frac{y}{\sin\theta}\right)\Bigg|_{y=z\cot\alpha+\frac{\sqrt{1-(NA/n)^2}}{\sin\alpha}} = \sin^{-1}\left|-\cot\alpha\cot\theta + \sqrt{1-\left(\frac{NA}{n}\right)^2}\csc\alpha\csc\theta\right|, \tag{13}$$

$$\phi_2(\theta) = \pi - \phi_1(\theta). \tag{14}$$

## Appendix B. The modification of Eq. (9) for faster numerical calculation

For the circular symmetric area $\Sigma_1$, the double integral can be reduced to a single integral as shown in [12,15]. For $\Sigma_2$, the integration area can be reduced by half due to the even symmetry of the bounds of $\phi$. These considerations lead to

$$I(x_\alpha, y_\alpha) = \left|\vec{K}+\vec{L}\right|^2 + \left|\vec{M}+\vec{N}\right|^2, \tag{15}$$

$$\vec{K} = \int_{\theta_C}^{\theta_{\max}}\int_{\phi_1(\theta)}^{\frac{\pi}{2}} \begin{pmatrix} 2\left(\sin^2\phi+\cos\theta\cos^2\phi\right)\cos(kx\sin\theta\cos\phi) \\ -2j(\cos\theta-1)\sin\phi\cos\phi\sin(kx\sin\theta\cos\phi) \\ -2j\sin\theta\cos\phi\sin(kx\sin\theta\cos\phi) \end{pmatrix} \times\cos^{\frac{1}{2}}\theta e^{iky_\alpha(\sin\alpha\cos\theta-\cos\alpha\sin\theta\sin\phi)}\sin\theta d\phi d\theta,$$

$$\vec{M} = \int_{\theta_C}^{\theta_{\max}}\int_{\phi_1(\theta)}^{\frac{\pi}{2}} \begin{pmatrix} -2j(\cos\theta-1)\sin\phi\cos\phi\sin(kx\sin\theta\cos\phi) \\ -2\left(\cos^2\phi+\cos\theta\sin^2\phi\right)\cos(kx\sin\theta\cos\phi) \\ 2\sin\theta\sin\phi\cos(kx\sin\theta\cos\phi) \end{pmatrix} \times\cos^{\frac{1}{2}}\theta e^{iky_\alpha(\sin\alpha\cos\theta-\cos\alpha\sin\theta\sin\phi)}\sin\theta d\phi d\theta,$$

$$\vec{L} = \pi\begin{pmatrix} I_0+I_2\cos\left(2\tan^{-1}(y_\alpha/x_\alpha\cos\alpha)\right) \\ I_2\sin\left(2\tan^{-1}(y_\alpha/x_\alpha\cos\alpha)\right) \\ -2iI_1\cos\left(2\tan^{-1}(y_\alpha/x_\alpha\cos\alpha)\right) \end{pmatrix}, \vec{N} = \pi\begin{pmatrix} I_2\sin\left(2\tan^{-1}(y_\alpha/x_\alpha\cos\alpha)\right) \\ I_0-I_2\cos\left(2\tan^{-1}(y_\alpha/x_\alpha\cos\alpha)\right) \\ -2iI_1\sin\left(2\tan^{-1}(y_\alpha/x_\alpha\cos\alpha)\right) \end{pmatrix},$$

$$I_0 = \int_0^{\theta_C}\cos^{\frac{1}{2}}\theta\sin\theta\left(1+\cos\theta\right)J_0\left(k\sqrt{x_\alpha^2+y_\alpha^2\cos^2\alpha}\sin\theta\right)e^{iky_\alpha\sin\alpha}d\theta,$$

$$I_1 = \int_0^{\theta_C}\cos^{\frac{1}{2}}\theta\sin^2\theta J_1\left(k\sqrt{x_\alpha^2+y_\alpha^2\cos^2\alpha}\sin\theta\right)e^{iky_\alpha\sin\alpha}d\theta,$$

$$I_2 = \int_0^{\theta_C}\cos^{\frac{1}{2}}\theta\sin\theta\left(1-\cos\theta\right)J_2\left(k\sqrt{x_\alpha^2+y_\alpha^2\cos^2\alpha}\sin\theta\right)e^{iky_\alpha\sin\alpha}d\theta.$$


## Acknowledgments

This work was supported by the Gordon and Betty Moore Foundation.